Research Square

Preprints are preliminary reports that have not undergone peer review.
They should not be considered conclusive, used to inform clinical practice,
or referenced by the media as validated information.

Loading path controls the seismic potential of strongly cemented healing faults

Changliang Wu
Yanshan University
Yiwen Ju
University of Chinese Academy of Sciences
Raza Ali
University of Houston
Yanjun Lu
Yanshan University
Yu Qi
Yanshan University
Jianchao Cai
China University of Petroleum, Beijing
Hongjian Zhu
zhj8641@163.com

Yanshan University

Article

Keywords: cemented faults, stress path, fault geometry, fault reactivation

Posted Date: November 5th, 2026

DOI: https://doi.org/10.21203/rs.3.rs-11355520/v1

License: This work is licensed under a Creative Commons Attribution 4.0 International License.
Read Full License

Additional Declarations: No competing interests reported.

Loading path controls the seismic potential of strongly cemented healing faults

Changliang Wu[a, †], Yiwen Ju[b, †], Ali Raza[c], Yanjun Lu[a], Yu Qi[a], Jianchao Cai[c, *], Hongjian Zhu[a, *]

[a]*School of Vehicle and Energy, Yanshan University, Qinhuangdao, 066000, China*

[b]*State Key Laboratory of Earth System Numerical Modeling and Application, College of Earth and Planetary Sciences, University of Chinese Academy of Sciences, Beijing 101408, China*

[c]*Department of Earth and Atmospheric Sciences, University of Houston, Houston, TX, 77204, USA*

[d]*State Key Laboratory of Petroleum Resources and Engineering, China University of Petroleum, Beijing 102249, China*

*** Corresponding author.**

E-mail addresses: caijc@cup.edu.cn (Jianchao Cai), zhj8641@163.com (Hongjian Zhu).

[†] Changliang Wu and Yiwen Ju contributed equally to this paper.

Abstract

The seismic potential of faults has traditionally been assessed on the basis of frictional properties and geometric configurations, a framework derived largely from studies of cohesionless faults. However, this framework may not apply to strongly cemented and healed faults, such as those filled with quartz or calcite veins, whose reactivation involves cohesive failure and off-fault damage rather than purely frictional sliding. Through triaxial experiments on precut sandstone and shale samples with varying fault dip angles, we show that stress path, rather than fault dip angle, dominates the seismic potential of fault reactivation. Under the load-weakening path that simulates normal faulting, the seismic moment released by strongly cemented faults is two orders of magnitude higher than that under the load-strengthening path that simulates reverse faulting, whereas variations in dip angle yield only a onefold to twofold difference. Remarkably, under the load-weakening path, the mechanically unfavorable 60° dip angle triggers the most violent instability. Rupture not only fractures the cement but also propagates into the surrounding rock, generating a supersized seismic moment and indicating significant energy overspill. We propose the rate of cement cohesion loss as the controlling mechanism. Rapid cohesion loss under the load-weakening path forces energy to overspill into the host rock, whereas slow loss under the load-strengthening path confines dissipation within the fault zone. Finally, the observation of nearly constant seismic moment across experiments with different unloading rates further supports the dominant role of stress path in controlling the seismic potential of fault reactivation.

Highlights:

- Seismic moment of cemented faults is stress path controlled, not geometry controlled.
- Unloading rate dictates fault rupture mode without changing seismic moment in healed

faults.

- A 60° unfavorable dip triggers the most violent rupture under load weakening path.
- Rapid cohesion loss forces energy overspill into host rock; slow loss confines dissipation.
- Tectonic stress path must be considered for seismic hazard assessment in extensional settings.

Keywords: cemented faults; stress path; fault geometry; fault reactivation

Introduction

During the earthquake recurrence cycle, the natural fault experiences a cycle of healing and reactivation rather than always being weakened[1,2]. Deep hydrothermal upwelling and anthropogenic fluid injection can significantly alter the physicochemical state of subsurface formations. Under elevated temperature and pressure conditions, prolonged mineral dissolution and precipitation enable the fault zone to achieve substantial cementation and healing through the filling of quartz-, calcite-, and other vein-type minerals[3,4,5,6,7,8], fully restoring or even surpassing its initial cohesiveness[9] (Fig. 1A). This is the final stage of fault strength recovery during the earthquake recurrence period. Large earthquakes frequently originate from these faults, which are extensively developed in plate borders, rift zones, and intraplate tectonically active places[10]. Strongly cemented healing faults in the crust are frequently created by the selective cementation of calcite and quartz[11]. For instance, secondary faults and cross-cutting veins, which are quartz or calcite veins that obliquely intersect with the fault zone at a specific angle[12] (Fig. 1B, C). The veins are not entirely filled along the fault plane, but they cut the fault and partially cement the nearby rocks on both sides. Cemented filling veins, in which the two fault walls are firmly “welded” together and the veins are fully filled along the fault plane to create a continuous “cemented film” or “cemented column”. According to Williams[13], these two forms are the results of the same healing process under various stress fields, fluid migration pathways, and time stages. For instance, several healing fissures filled with quartz veins were discovered during deep drilling of the San Andreas fault. High temperature fluid-assisted healing is a crucial process for the recovery of fault strength, as evidenced by the formation of calcite veins in the fault zone[7,14,15] (Fig. 1D). Normal faults typically experience periodic cementation healing in extensional tectonic environments like the East African Rift and the Rio Grande Rift[16].

The rate-state friction law serves as the foundation for most of the current fault mechanic research. According to Kang[17], Brace[18], and Scholz[19], this concept effectively explains the sliding instability behavior of cohesionless or weak cohesion faults, such as gouge and unconsolidated breccia. However, the key assumption of this approach is that the fault is a cohesiveless frictional contact, which is fundamentally challenged in heavily cemented healing faults[20]. The latter instability must

include brittle cement fracture and cohesiveness loss rather than simple friction sliding. Because of this mechanism discrepancy, the classic friction law may not completely represent the seismic nucleation process[3]. Meanwhile, there is still a dearth of systematic research on the mechanical behavior and seismic potential of strongly cemented faults with significant or even complete recovery of cohesion, as the majority of current experimental studies concentrate on uncemented or weakly cemented materials[3,14,21,22] (such as quartz powder and volcanic ash rapid precipitation) (Fig. S1).

It is well known that different loading paths commonly occur in natural fault zones. Load-strengthening path (LSP) is commonly associated to reverse faults (in the absence of significant fluid pressure increase) and load-weakening path (LWP) to normal faults[23]. The fault dip angle, or the angle between the fault plane and the regional principal stress, is thought to be the main factor controlling the difficulty of its activation in the traditional fault seismic potential assessment[24,25,26]. Seismic risk assessment makes extensive use of the Mohr-Coulomb framework's "dominant angle" (~ 30 °) and "inferior angle" (~ 60 °) ideas[27]. Nonetheless, this framework's underlying assumption is that the fault is always in a comparable stress loading history. Do the historical stress paths encountered by natural faults, such as unloading confining pressure induced by uplift and pressurization caused by burial (transformation of tectonic compression and extension), influence their activation behavior? This topic has not received much attention in recent years[21,28,29,30]. There is also a dearth of experimental study to determine if the reactivation process is still subject to geometric control or may be subverted by the stress route, particularly for firmly cemented defects that have undergone full healing. According to Del[31], Petruccelli[32], and Schorlemmer[33], the normal faults in the basin's basement may experience a stress path shift from tension to compression in the later inversion structure. This implies that one important factor influencing the reactivation behavior of faults might be the historical stress route.

Because of the technical limitations of laboratory methods, there are still few systematic studies on the activation of strongly cemented faults in research laboratories despite these doubts and evidence[34,35,36]. The difficulty to duplicate the geological time scale of hundreds to thousands of years necessary for robust cementation processes is the primary emphasis of these limitations. To get around these issues, the prefabricated fault surface was cemented with epoxy resin to mimic the potent cementation healing effect of quartz and calcite veins. As a repeatable and controllable mechanical behavior simulation material, epoxy resin may successfully simulate the initial state of the fault with significant recovery of cohesiveness despite the material variances between it and natural minerals[37]. Bypassing the limitations of geological time scales, it enables us to concentrate on controlling reactivation processes through fault geometry and historical stress courses. We extensively investigated the impact of fault geometry dip angles and historical stress courses on the seismic potential of heavily cemented healing faults using a combination of macroscopic

mechanical tests and microstructure characterisation. This study provides a new experimental basis and mechanical criterion that must be included in the constraint of "structural stress path" to evaluate the seismic risk of strongly cemented faults in tensile tectonic environments.

Material and methods

We performed triaxial saw-cut experiments with cylindrical samples of Zizhong sandstone (74.9% quartz, 18.5% feldspar, ~6.1% clay, and 0.5% calcite[38]) with saw-cut oriented at 0°, 30°, 60°, and 90° to the sample axis. The sawing surface was polished using the same sandpaper mesh to remove the impact of section roughness[39]. The polished surface was then uniformly coated with epoxy resin, and the fault upper and lower rock masses were completely compressed to create a cemented layer that was roughly 1 mm thick[37]. To make sure the fault was completely cemented and healed, the initial fault samples were placed in the steel groove clamp and allowed to cure for roughly 15 days. The TAW-2000 rock mechanics test equipment, which has an injection pump to regulate pore fluid pressure and a Hoek-type confining chamber[40] (Fig. 2A), was used to conduct triaxial loading testing. We carried out numerous pre-experiments and chose the highest compressive strength determined by each fault dip angle sample as the screening standard in order to lessen the discreteness of the cementation impact throughout the sample preparation procedure. For formal experiments, only the samples exhibiting the most stable mechanical behavior and the highest cementation healing effect were chosen.

To reproduce different tectonic loading paths, we alternatively increased the axial stress (σ_1) to simulate LSPs or decreased the confining pressure (σ_3), to simulate LWPs[40,41,42,43] (Fig. 2B). In order to achieve the predetermined starting stress condition, the sample was hydrostatically loaded at a rate of 0.033 MPa/s to the target σ_3 for LSPs and the target σ_1 for LWPs. An initial confining pressure of 50 MPa was first applied. Subsequently, the axial stress was raised to 90% of the peak strength. Upon confirmation of system stability, the experiment proceeded along two distinct paths: increasing the axial stress (LSP) and unloading the confining pressure (LWP), both continued until the onset of fault instability[21].

To ensure that the experimental results reflect the effect of stress path alone, we first conducted a series of LWP experiments at unloading rates ranging from 0.01 to 0.15 MPa/s (Fig. S2). The results show that the laboratory seismic moment remains nearly constant across this range, indicating that the reactivation potential of strongly cemented faults is not significantly influenced by loading rate within the range investigated (Fig. S3). Accordingly, an unloading rate of 0.05 MPa/s was selected for LWP experiments. Representative samples were chosen at the conclusion of the experiment to preserve the fault plane in order to examine the microstructure of the cement in the fault zone. Simultaneously, we conducted a comparative test on the strong heterogeneous shale under the same experimental settings in order to improve the reliability of the experimental data.

Figure S4 in Supplementary Materials displays the preparation procedure and pictures of the pertinent samples. The detailed experimental design is shown in Table 1.

Results

Basic mechanical characteristics of faults

Our experimental results demonstrate significant differences in mechanical strength and post-peak behavior of strongly cemented, healed faults as a function of fault dip angle and historical stress path (Fig. 3A). Under the LSP path, the boundary condition faults (0° and 90°) exhibited the highest and lowest mechanical strengths, respectively, while the inclined faults (30° and 60°) were bounded between them. The 30° fault entered a stable slip regime after peak strength, whereas the 60° fault maintained only a brief period of stable slip before undergoing rapid failure (Fig. 3C, D). The post-peak modulus and stress drop rate can serve as preliminary indicators of the rate of cement cohesion loss, which aligns with the Coulomb-Mohr criterion's description of favorable and unfavorable fault dip behavior[27]. In contrast, under the LWP path, this mechanical pattern is reversed: the instability strengths of the boundary dip faults are bounded by those of the inclined faults. The favorably oriented fault (30°) was the first to fail under relatively small pore-pressure perturbations, whereas the unfavorably oriented fault (60°) required the highest pore-pressure threshold to reach instability (Fig. 3B). Moreover, the magnitude of the stress drops at instability also showed marked dip-dependent variation. These results indicate that the reactivation susceptibility and seismic potential of strongly cemented faults remain predominantly governed by the favorably oriented fault geometry as described by the Mohr-Coulomb criterion. Subsequently, we performed further statistical analysis of these mechanical parameters and results, and constructed Mohr circles for inclined faults under different stress paths, incorporating the stress states at failure for boundary dip faults.

The variation in stress drop magnitude remained nearly consistent, unaffected by differences in the stress path, indicating that it is strictly governed by the fault geometric dip (Fig. 3E). This trend aligns with the favorable and unfavorable dip framework defined by the Mohr-Coulomb criterion, as observed for the basic mechanical parameters: under favorable dip conditions (30°), the stress drop after fault instability is significantly smaller. Similarly, the critical pore pressure for triggering instability under the LWP path is also controlled by fault geometry; at a favorable dip (30°), instability occurs under very low pore-pressure perturbation (11 MPa). We further analyzed the position and size of the Mohr circles for the inclined faults, revealing a strong correlation between the failure condition and both the fault dip and the stress path (Fig. 3F). For a given fault dip, the LWP path shifts the Mohr circle to the left, whereas under a fixed stress path, increasing the fault dip significantly enlarges the area of the Mohr circle. This indicates that both the fault geometric dip and the stress path substantially influence the risk of fault instability. Under the LWP path, the Mohr circle not only shifts leftward but also expands, whereas under the LSP path, no leftward shift is observed. This further suggests that the reactivation of strongly cemented faults is more sensitive

to the stress path than to the fault geometric dip. The detailed calculation results are shown in Table 2.

Instability behavior after fault activation

We analyzed the post-instability failure modes of the faults (Fig. S5). The failure modes of strongly cemented faults vary markedly under different stress paths. For horizontal faults (90°) and favorably oriented faults (30°), the stress path has little influence on their failure modes. Horizontal faults are dominated by axial compression and deformation of the surrounding host rock in both the hanging wall and footwall, indicated by the development of distinct white conjugate shear bands. In contrast, favorably oriented faults are governed primarily by frictional sliding along the fault surfaces. However, the stress path significantly influences the failure modes for vertical faults (0°) and unfavorably oriented faults (60°). For vertical faults, failure transitions from tensile fracturing under the LSP path to brittle shear fracturing under the LWP path. For unfavorably oriented faults, failure evolves from frictional slip along localized shear zones under the LSP path to a compound failure mode under the LWP path, involving slip along the fault plane coupled with brittle fracturing of the host rock in both the hanging wall and footwall. Correspondingly, the energy release pattern of the fault system shifts from localized energy dissipation via failure of the cemented fault core to pervasive shear-driven energy dissipation that breaches the cemented core and propagates into the surrounding rock. This transition indicates a marked energy spillover effect within the system[44]. These observations further suggest that, compared to fault geometry, the stress path may exert a more dominant control on the failure behavior and seismic potential of strongly cemented faults. Furthermore, comparative tests conducted on bedded shale under identical conditions reveal that the stress-path-induced differences in failure modes are even more pronounced in shale. Additional details and failure mode diagrams are provided in Fig. S5C, D.

Microstructural analysis of cemented mass

Based on microstructural observations of the post-failure cemented fault surfaces, we further analyzed the influence of stress path and fault geometric dip on the failure mechanisms of the fault system (Fig. 4A). In terms of fault geometry, the damage distribution within the cemented material on low-angle (favorably oriented, 30° dip) fault planes is more uniform compared to that on high-angle faults. In contrast, high-angle (60° dip) fault cement exhibits significant cement cracking and even cataclasis (similar to fault brecciation[45,46] and observed in some friction experiments[36,47]). A similar phenomenon was also observed in our supplementary shale experiments (Fig. 4B). From the perspective of stress path, the low-angle fault exhibits no significant change, whereas the cemented material on the high-angle fault plane shows a certain degree of damage intensification. To further investigate this, we quantified the surface roughness and multifractal spectrum of the fault planes and performed detailed data analysis (Fig. 5). We found that the surface roughness of the cemented material on the low-angle fault is more homogeneous, with a narrower multifractal spectrum width, indicating more uniform damage distribution without pronounced damage localization or stress concentration[48]. In contrast, the cemented surface of the high-angle fault is considerably rougher,

with a significantly broader multifractal spectrum width than that of the low-angle fault. This suggests that the cement on the high-angle fault has undergone a marked localized damage process. This is likely due to the unfavorable geometric dip placing the fault under a state of higher shear and normal stress (Fig. S6). As the fault dip increases, the mechanical response of the cement transitions from compaction strengthening under low normal stress to crushing weakening under high normal stress[49]. Furthermore, increased shear stress drives local stress concentration within the cement, leading to its tearing and fragmentation as frictional slip progresses[50]. Building on the aforementioned mechanical characteristics of the faults (stress drop magnitude) and their failure modes, where energy is either localized within the cemented fault core or spills over, breaching the core into the surrounding host rock. We further hypothesize that the system-level energy release mode of strongly cemented, healed faults may be governed by the rate of cohesion loss within the cement. This, in turn, likely influences their seismic potential upon reactivation. Specifically, rapid cohesion loss (LWP path) prevents the fault zone from sufficiently dissipating the accumulated strain energy, forcing it to spill over into the host rock. In contrast, slow cohesion loss (LSP path) confines energy dissipation primarily within the fault zone itself.

Discussion

Seismic potential assessment of strongly cemented, healed faults

Based on the experimental data, we calculated the seismic moment and magnitude for the dipping faults (Figs. 6, 7C). The cumulative deformation moment (including both seismic and aseismic components) is given by[51]:

$$M_0 = GA\,\Delta s \qquad (1)$$

where A is the total fault area (30°: ~3,925 mm^2 and 60°: ~2,267 mm^2 for the elliptical fault plane used in this study), and G is the shear stiffness. The slip displacement is calculated by converting the axial strain and the geometric dip angle of the fault. Along the LWP path, fault displacement involved slip along a preexisting cemented plane as well as propagation of a new fracture surface. Consequently, the total fault area was increased by the area of this newly formed fracture surface (~6,192 mm^2). Δs is fault slip displacement. Figure S7 presents the experimental results of fault slip under different unloading rates. The results show that the instantaneous relative slip displacement varies only slightly across different unloading rates (within 1 mm), and consequently, the instantaneously released seismic moment remains relatively constant.

Figure 7C illustrates the temporal evolution of the deformation moment. It is evident that both the stress path and the fault dip angle significantly influence the seismic moment of strongly cemented faults; however, the magnitude of their respective influence differs markedly. Most notably, the stress path predominantly controls the magnitude of the seismic moment: the moment released under the LWP path is approximately two orders of magnitude greater than that under the LSP path ($\Delta \log Mw \approx 2.6$). In contrast, within the same stress path, variations in dip angle (e.g., 30° vs. 60°) result in only a 1- to 2- fold difference in seismic moment, which is considerably smaller

than the effect of the stress path. Particularly significant is the observation that, under the LWP path, the unfavorably oriented (60° dip) fault experienced rupture that breached the cemented fault core and propagated into the surrounding host rock, forming a through-going shear zone. This process generated an exceptionally large seismic moment. Approximately double that of the favorably oriented fault. This anomalous phenomenon indicates that, under the unloading confining pressure conditions, the system underwent a significant energy spillover effect. The cemented fault core itself became insufficient to dissipate the accumulated strain energy, forcing the rupture to extend into the adjacent host rock. We observed consistent results in supplementary experiments conducted on shale (Fig. S8), reinforcing the dominant role of the stress path in controlling the reactivation seismic potential of strongly cemented, healed faults.

Figure 6 compares the moment magnitude estimated in this study with the moment magnitude predicted from the rupture area of natural faults, based on the empirical relation[52]:

$$\boldsymbol{M_w = 4.07 + 0.98\, log(A)} \qquad (2)$$

The moment magnitude of stick‐slip events is also calculated from the seismic moment using[53]:

$$\boldsymbol{M_w = 2/3\, log\, M_0 - 6.06} \qquad (3)$$

The M_W values derived from seismic moment are slightly higher than those predicted from the rupture area, yet they remain within the confidence bounds of natural earthquake distributions[52,54,55,56]. This demonstrates that the system-level energy release mode of strongly cemented, healed faults govern their seismic potential[57]. The stress path and fault dip angle regulate the rate of cement cohesion loss, thereby controlling whether the fault system dissipates energy locally within the fault core or via rupture that breaches the core and propagates into the surrounding host rock.

Stress path dependence of seismic potential in strongly cemented, healed faults

Utilizing the rapid cementation capability of epoxy resin to form strongly healed fault zones, we investigated the influence of fault stress path history and geometric dip angle on the seismic potential of reactivated, strongly cemented faults. Cementation effects are negligible over short holding times but become dominant over prolonged periods[3]. This indicates that when a fault undergoes long-term cementation healing, its behavior during re-strengthening and re-shearing reflects a combination of enhanced shear dilatancy at cemented contacts and the fracturing of cohesive strength[36,58]. Therefore, the key to understanding the seismic potential of strongly cemented faults lies in quantifying the rate of cohesion loss within the cement during the failure process and linking it to the fault system's energy release mode (Fig. 7). We provide clear evidence establishing that the stress path plays a dominant role in controlling the seismic potential of strongly cemented, healed faults upon reactivation. Under the LWP path, strongly cemented faults release a seismic moment approximately two orders of magnitude greater than under the LSP path ($\Delta \log Mw \approx 2.6$), whereas variations in dip angle result in only a 1- to 2- fold difference in seismic moment. In our supplementary experiments, the seismic moment associated with the reactivation of strongly cemented faults remains relatively constant and does not vary significantly with the

unloading rate. This finding further supports the dominant role of loading path in controlling the reactivation potential of strongly cemented faults, as established in this study.

We quantified the rate of cohesion loss using the slope ($K = d\sigma/dt$) of the post-peak stress drop phase on the stress-time curve (Fig. 7A). This approach is based on the reasoning that during the instability, the drop in shear stress is primarily contributed by the loss of cohesion within the cement, with both exhibiting identical time-varying characteristics[3]. It should be noted that the magnitude of the stress drop itself is influenced by the fault's frictional healing history[59,60]. However, this study focuses on the rate rather than the magnitude, revealing the control exerted by the stress path on instability dynamics. The results demonstrate that the stress path exerts a significantly stronger control over the cohesion loss rate than the fault dip angle. The average cohesion loss rate under the LWP path is approximately three orders of magnitude higher than that under the LSP path ($\Delta \log C \approx 2.98$), whereas variations due to geometric dip are less than twofold. This substantial difference suggests that under the LWP path, cohesion within the fault zone is lost in a burst-like, rapid manner, laying the groundwork for subsequent energy spillover within the fault system.

The difference in the rate of cohesion loss is directly reflected in the post-activation evolution of the friction coefficient (Fig. 7B), which in turn indicates the energy release mode of the fault system[61]. Under the LSP path, the sliding friction coefficient after fault activation is significantly higher and decreases more gradually compared to that under the LWP path. Particularly for favorably oriented faults (30°), the coefficient remains almost constant at a residual level after activation, suggesting that the system's energy is dissipated in a stable, localized manner within the cemented fault core (Fig. 7B, blue dashed line). This observation aligns perfectly with the instability mode described in Section 3.2, where rupture is confined to the fault zone. In contrast, under the LWP path, the friction coefficient drops sharply after activation. While energy release remains localized within the fault core for favorably oriented faults, a distinct two-stage behavior is observed for unfavorably oriented faults (60°): the friction coefficient first undergoes a rapid drop, followed by a period of stable sliding, before a second abrupt drop occurs (Fig. 7B, blue solid line). This two-stage behavior corresponds precisely to the failure process observed in Section 3.2—initial rapid cohesion loss within the fault core, followed by energy spillover driving through-going shear fracturing in the surrounding rock. The transition from purely frictional instability to a combined frictional-fracturing failure mode introduces a second critical slip distance, a phenomenon also reported in previous experiments on healed faults[34,36,58].

Finally, we compared the rate of cohesion loss and the corresponding seismic moment under all experimental conditions (Fig. 8). Regardless of the loading rate or lithology, the rate of cement cohesion loss during reactivation of strongly cemented faults under LWP is significantly higher than that under LSP (Fig. 8A). The corresponding seismic moments show the same evolutionary trend (Fig. 8B).

In summary, we propose that the rate of cohesion loss within the fault core serves as a key governing parameter for the seismic potential of strongly cemented, healed faults. Rapid cohesion

loss (LWP path) prevents the fault zone from dissipating the accumulated strain energy at its own scale, forcing energy to spill over into the surrounding rock and driving through-going shear failure, thereby releasing an exceptionally large seismic moment. In contrast, slow cohesion loss (LSP path) localizes energy dissipation within the fault core, resulting in a limited seismic moment.

Implications for seismicity

Traditional seismic hazard assessment frameworks heavily rely on geometric criteria, where the angle between the fault dip and the regional principal stress is considered as the primary factor controlling both the likelihood of reactivation and the magnitude of seismic events[25,26]. However, this study suggests that for strongly cemented faults that have undergone long-term healing, this geometry-centered paradigm may require revision. We find that under the LWP (normal-faulting) path, the classic "unfavorable" dip of 60° releases an anomalously large seismic moment, whereas the instability scale of the "favorable" 30° dip fault is relatively limited. This indicates that for the reactivation of strongly cemented, healed faults, the historical stress path may be more decisive than the geometric orientation. Therefore, incorporating the "tectonic stress path" into seismic hazard assessment frameworks is essential for accurately evaluating the seismic risk posed by such strongly cemented faults.

In nature, normal faults in extensional tectonic settings (e.g., the East African Rift, the Rio Grande Rift, and the North Sea Basin) sometimes exhibit unexpectedly large displacements and seismic moments that are mismatched with their geometric scales[16]. This phenomenon has been difficult to explain with traditional frictional sliding theory. The "energy spillover" mechanism proposed in this study provides a new mechanical explanation. When strongly cemented, healed faults experience a reduction in confining pressure (e.g., due to uplift, denudation, or extension), rapid cohesion loss in the cement may cause the stored elastic strain energy in the system to exceed the dissipation capacity of the fault zone itself. This forces the rupture to propagate into the surrounding host rock, thereby releasing an anomalously large seismic moment. The transition in the failure mode of such faults from purely frictional to a combination of friction and fracturing introduces a second critical slip distance, a phenomenon that has been widely reported in other studies[34,36,58]. This mechanism suggests that strongly cemented faults in extensional tectonic regions that have undergone significant uplift or extension histories may have an underestimated seismic potential.

The seismic recurrence cycle can be conceptualized as an alternating sequence of fault healing (strength recovery) and rupture (energy release)[25,62]. While traditional models have focused primarily on strength accumulation during the healing phase and frictional sliding during rupture, the mechanisms governing energy partitioning during the re-rupture of healed faults remain poorly understood[3,63]. This study demonstrates that the energy-release mode of strongly cemented faults upon reactivation is controlled by the rate of cohesion loss within the cemented fault core: rapid loss triggers energy spillover, driving fracture propagation into the surrounding host rock and generating anomalously large seismic events; slow loss, in contrast, localizes energy dissipation within the fault core, resulting in limited seismic moment. This finding implies that both the degree of fault healing

(i.e., the level of cohesion recovery within the fault zone) and the stress path during reactivation jointly determine the partitioning of energy in the seismic cycle. Specifically, the proportions allocated to overcoming friction, breaking the cement, and shearing the host rock. These insights provide a new experimental perspective for building a more comprehensive energy-budget model for earthquakes, although systematic energy-partitioning analysis was not conducted in this study.

The conceptual framework proposed in this study yields several testable predictions. For example, in extensional tectonic settings that have undergone significant uplift history (e.g., rift shoulders, passive continental margins), if a fault zone shows evidence of strong healing via quartz or calcite vein infilling[7,9], its seismic potential may be underestimated by traditional geometry-based assessment methods. Conversely, if a fault has experienced a history of continuous burial or compression, its seismic potential may align more closely with traditional expectations. Future research could test this prediction by comparing the actual seismic activity of strongly cemented faults in different tectonic settings. Furthermore, the concept of "cohesion loss rate" highlighted in this study suggests that laboratory-scale measurements of the post-peak brittle behavior of fault rocks could provide a new lithological parameter for evaluating the seismic potential of natural faults.

Conclusions

This study conducted triaxial experiments on prefabricated sandstone sections bonded with epoxy resin, systematically revealing the core controlling factors and seismic potential of the reactivation process of strongly bonded healing faults (simulated quartz/calcite vein filled faults). The results show that the stress path dominates the scale of instability and can override geometric control. The seismic moment released by strongly cemented faults under the LWP path is about two orders of magnitude greater than that under the LSP path, while dip angle variations result in only a 1- to 2-fold difference. Crucially, under the LWP path, the 60° fault, classically considered a mechanically "unfavorable" dip, triggered the most intense instability, with rupture breaching the cemented fault core and propagating into the surrounding host rock, forming through going shear fractures and releasing an anomalously large seismic moment. This indicates a marked energy spillover effect within the system. We propose the "rate of cohesion loss within the cement" as a key governing parameter: rapid cohesion loss (LWP path) prevents the fault zone from dissipating the accumulated strain energy, forcing it to spill over into the host rock, whereas slow cohesion loss (LSP path) confines energy dissipation within the fault core. This mechanism provides a new mechanical explanation for large displacement normal fault earthquakes in extensional tectonic settings (e.g., rift systems, passive continental margins, and regions of differential uplift), suggesting that the seismic potential of strongly cemented, healed faults that have undergone significant uplift or extensional history may be underestimated by traditional geometry assessment methods. Moreover, this study reveals a fundamental distinction between the reactivation behavior of strongly cemented

faults and the classical frictional slip framework. The former is dominated by cohesion loss driven brittle fracturing and energy spillover, while the latter is governed primarily by frictional dissipation. This highlights the need for future fault mechanics research to distinguish between "friction dominated" and "cohesion breakdown dominated" instability modes, and to incorporate the "tectonic stress path" into seismic hazard assessment frameworks.

Data availability

Data will be made available on request.

References

1. Zhao, Z., Xue, L., Bürgmann, R., Heimisson, E. R., Lu, W., & Yue, H. (2025). Tidal and hydrological seismicity modulations reveal pore fluid diffusion during earthquake nucleation. Science Advances, 11(49), eady6350. https://doi.org/10.1126/sciadv.ady6350
2. Bos, B., and C.J. Spiers. "Effect of Phyllosilicates on Fluid-Assisted Healing of Gouge-Bearing Faults." Earth and Planetary Science Letters 184, no. 1 (2000): 199–210. https://doi.org/10.1016/s0012-821x(00)00304-6.
3. Volpe, R. Affinito, L. Calzolari, G. Pozzi, C. Marone, C. Collettini, The influence of cementation on fault stability, Earth and Planetary Science Letters, Volume 671, 2025, 119674, ISSN 0012-821X, https://doi.org/10.1016/j.epsl.2025.119674.
4. Yasuhara, Hideaki, Chris Marone, and Derek Elsworth. "Fault Zone Restrengthening and Frictional Healing: The Role of Pressure Solution." Journal of Geophysical Research: Solid Earth 110, no. B6 (2005). Portico. https://doi.org/10.1029/2004jb003327.
5. Ujiie, Kohtaro, Hanae Saishu, Åke Fagereng, et al. "An Explanation of Episodic Tremor and Slow Slip Constrained by Crack-Seal Veins and Viscous Shear in Subduction Mélange." Geophysical Research Letters 45, no. 11 (2018): 5371–79. Portico. https://doi.org/10.1029/2018gl078374
6. Mozley, Peter S., and Laurel B. Goodwin. "Patterns of Cementation along a Cenozoic Normal Fault: A Record of Paleoflow Orientations." Geology 23, no. 6 (1995): 539. https://doi.org/10.1130/0091-7613(1995)023<0539:pocaac>2.3.co;2
7. Williams, Randolph T., Peter S. Mozley, Warren D. Sharp, and Laurel B. Goodwin. "U-Th Dating of Syntectonic Calcite Veins Reveals the Dynamic Nature of Fracture Cementation and Healing in Faults." Geophysical Research Letters 46, no. 22 (2019): 12900–12908. Portico. https://doi.org/10.1029/2019gl085403.
8. Lee, Young-Joon, David V. Wiltschko, Ethan L. Grossman, John W. Morse, and William M. Lamb. "Sequential Vein Growth with Fault Displacement: An Example from the Austin Chalk Formation, Texas." Journal of Geophysical Research: Solid Earth 102, no. B10 (1997): 22611–28. Portico. https://doi.org/10.1029/97jb01945.

9. Bradbury, K.K., D.C. Barton, J.G. Solum, S.D. Draper, and J.P. Evans. “Mineralogic and Textural Analyses of Drill Cuttings from the San Andreas Fault Observatory at Depth (SAFOD) Boreholes: Initial Interpretations of Fault Zone Composition and Constraints on Geologic Models.” Geosphere 3, no. 5 (2007): 299. https://doi.org/10.1130/ges00076.1.
10. Ikari, Matt J., Brett M. Carpenter, Christoph Vogt, and Achim J. Kopf. “Elevated Time-Dependent Strengthening Rates Observed in San Andreas Fault Drilling Samples.” Earth and Planetary Science Letters 450 (September 2016): 164–72. https://doi.org/10.1016/j.epsl.2016.06.036.
11. Pizzati, Mattia, Fabrizio Balsamo, Fabrizio Storti, and Paola Iacumin. “Physical and Chemical Strain-Hardening during Faulting in Poorly Lithified Sandstone: The Role of Kinematic Stress Field and Selective Cementation.” GSA Bulletin 132, nos. 5–6 (2019): 1183–200. https://doi.org/10.1130/b35296.1.
12. Raimbourg, H., Rajič, K., Moris-Muttoni, B., Famin, V., Palazzin, G., Fisher, D., et al. (2021). Quartz vein geochemistry records deformation processes in convergent zones. Geochemistry, Geophysics, Geosystems, 22, e2020GC009201. https://doi.org/10.1029/2020GC009201
13. Williams, Randolph T., John R. Farver, Charles M. Onasch, and Daniel F. Winslow. “An Experimental Investigation of the Role of Microfracture Surfaces in Controlling Quartz Precipitation Rate: Applications to Fault Zone Diagenesis.” Journal of Structural Geology 74 (May 2015): 24–30. https://doi.org/10.1016/j.jsg.2015.02.011.
14. Aben, F. M., M.-L. Doan, J.-P. Gratier, and F. Renard. “Experimental Postseismic Recovery of Fractured Rocks Assisted by Calcite Sealing.” Geophysical Research Letters 44, no. 14 (2017): 7228–38. Portico. https://doi.org/10.1002/2017gl073965.
15. Guglielmi G, DI TORO G, TESEI T. Temperature dependence of fault frictional healing in quartz gouges at hydrothermal conditions [J]. Journal of Geophysical Research: Solid Earth, 2026, 131: e2025JB033637.
16. Calais, Eric, Nicolas d’Oreye, Julie Albaric, et al. “Strain Accommodation by Slow Slip and Dyking in a Youthful Continental Rift, East Africa.” Nature 456, no. 7223 (2008): 783–87. https://doi.org/10.1038/nature07478.
17. Kang, J., Lucas, A., Mangeney, A. *et al.* Frictional weakening in the highly mobile 2025 Blatten rock and ice avalanche in Switzerland. *Commun Earth Environ* **7**, 722 (2026). https://doi.org/10.1038/s43247-026-03983-1
18. Brace, W., & Byerlee, J. (1966). Stick-slip as a mechanism for earthquakes. Science, 153(3739), 990–992. https://doi.org/10.1126/science.153.3739.990
19. Scholz, C. H. (1998). Earthquakes and friction laws. Nature, 391(6662), 37–42. https://doi.org/10.1038/34097
20. Boulton, C., Moore, D. E., Lockner, D. A., Toy, V. G., Townend, J., & Sutherland, R. (2014). Frictional properties of exhumed fault gouges in DFDP-1 cores, Alpine Fault, New Zealand. Geophysical Research

Letters, 41(2), 356–362. https://doi.org/10.1002/2013GL058236

21. Giorgetti, C., & Violay, M. (2021). The influence of loading path on fault reactivation: A laboratory perspective. Geophysical Research Letters, 48, e2020GL091466. https://doi.org/10.1029/2020GL091466

22. Olsen, Martin P., Christopher H. Scholz, and Albert Léger. “Healing and Sealing of a Simulated Fault Gouge under Hydrothermal Conditions: Implications for Fault Healing.” Journal of Geophysical Research: Solid Earth 103, no. B4 (1998): 7421–30. Portico. https://doi.org/10.1029/97jb03402.

23. Sibson, R. H. (1993). Load-strengthening versus load-weakening faulting. Journal of Structural Geology, 15(2), 123–128. https://doi.org/10.1016/0191-8141(93)90090-W

24. Lee, J., Tsai, V. C., Hirth, G., Chatterjee, A., and Trugman, D. T.: Fault-network geometry influences earthquake frictional behaviour, Nature, 10.1038/s41586-024-07518-6, 2024.

25. Liu, M., Tan, Y. J., Guo, H., Li, H., Lu, R., and Jiang, J.: Fluids and fault structures underlying the complex foreshock sequence of the 2021 Mw 6.1 Yangbi earthquake, Earth and Planetary Science Letters, 651, 10.1016/j.epsl.2024.119173, 2025.

26. Sibson, R. H. (1985). A note on fault reactivation. Journal of Structural Geology, 7(6), 751–754. https://doi.org/10.1016/0191-8141(85)90150-6

27. Labuz, Joseph F., and Arno Zang. “Mohr–Coulomb Failure Criterion.” Rock Mechanics and Rock Engineering 45, no. 6 (2012): 975–79. https://doi.org/10.1007/s00603-012-0281-7.

28. Olive, Jean-Arthur, Mark D. Behn, and Luca C. Malatesta. “Modes of Extensional Faulting Controlled by Surface Processes.” Geophysical Research Letters 41, no. 19 (2014): 6725–33. Portico. https://doi.org/10.1002/2014gl061507.

29. Pinzuti, Paul, Arnaud Mignan, and Geoffrey C.P. King. “Surface Morphology of Active Normal Faults in Hard Rock: Implications for the Mechanics of the Asal Rift, Djibouti.” Earth and Planetary Science Letters 299, nos. 1–2 (2010): 169–79. https://doi.org/10.1016/j.epsl.2010.08.032

30. Ring, Uwe, Christian Betzler, and Damian Delvaux. “Normal vs. Strike-Slip Faulting during Rift Development in East Africa: The Malawi Rift.” Geology 20, no. 11 (1992): 1015. https://doi.org/10.1130/0091-7613(1992)020<1015:nvssfd>2.3.co;2.

31. Del Ventisette, Chiara, Domenico Montanari, Federico Sani, and Marco Bonini. “Basin Inversion and Fault Reactivation in Laboratory Experiments.” Journal of Structural Geology 28, no. 11 (2006): 2067–83. https://doi.org/10.1016/j.jsg.2006.07.012.

32. Petruccelli, A., Schorlemmer, D., Tormann, T., Rinaldi, A. P., Wiemer, S., Gasperini, P., & Vannucci, G. (2019). The influence of faulting style on the size-distribution of global earthquakes. Earth and Planetary Science Letters, 527, 115791. https://doi.org/10.1016/j.epsl.2019.115791

33. Schorlemmer, D., Wiemer, S., & Wyss, M. (2005). Variations in earthquake-size distribution across different stress regimes. Nature, 437, 539–542. https://doi.org/10.1038/nature04094

34. Muhuri, T.A. Dewers, T.E. Scott Jr, Z.E Reches. Interseismic fault strengthening and earthquake-slip

instability: friction or cohesion? Geology, 31 (10) (2003), pp. 881-884

35. Nakatani, C.H. Scholz. Frictional healing of quartz gouge under hydrothermal conditions: 1. Experimental evidence for solution transfer healing mechanism. J. Geophys. Res.: Solid Earth, 109 (B7) (2004)

36. Tenthorey, S.F. Cox. Cohesive strengthening of fault zones during the interseismic period: an experimental study. J. Geophys. Res.: Solid Earth, 111 (B9) (2006)

37. Srivastava, A. K., and Pragyan Mohan. “Synthesis, Reactions, and Properties of Modified Epoxy Resins.” Journal of Macromolecular Science, Part C: Polymer Reviews 37, no. 4 (1997): 687–716. https://doi.org/10.1080/15321799708009653.

38. Chen LX, Wei-yao Guo, Dong-xiao Zhang, Tong-bin Zhao, Experimental study on the influence of prefabricated fissure size on the directional propagation law of rock type-I crack, International Journal of Rock Mechanics and Mining Sciences, Volume 160, 2022, 105274, ISSN 1365-1609, https://doi.org/10.1016/j.ijrmms.2022.105274.

39. Song, J., Wang, L., Dresen, G., Martínez- Garzón, P., Vavryčuk, V., Bohnhoff, M., et al. (2025). Laboratory acoustic emissions reveal stress rotation from preparation processes toward fault slip on varying surface roughness in granular materials. Geophysical Research Letters, 52, e2024GL113093. https://doi.org/10.1029/2024GL113093.

40. Noël, C., Passelègue, F. X., Giorgetti, C., & Violay, M. (2019). Fault reactivation during fluid pressure oscillations: Transition from stable to unstable slip. Journal of Geophysical Research. Solid Earth, 124, 10940–10953. https://doi.org/10.1029/2019JB018517

41. Han X, Wang L, Rybacki E, et al. A comparison of porous sandstone fracturing induced by increasing fluid pressure or decreasing confining pressure: Stress-path and rate-dependence effects[J]. Journal of Rock Mechanics and Geotechnical Engineering, 2025

42. French, M. E., Zhu, W., & Banker, J. (2016). Fault slip controlled by stress path and fluid pressurization rate. Geophysical Research Letters, 43, 4330–4339. https://doi.org/10.1002/2016GL068893

43. Passelègue, F. X., Almakari, M., Dublanchet, P., Barras, F., Fortin, J., & Violay, M. (2020). Initial effective stress controls the nature of earthquakes. Nature Communications, 11, 5132. https://doi.org/10.1038/s41467-020-18937-0

44. Wu CL, Zhu HJ, Ju YW, Hu ZQ, Lu YJ, Raza A, Cai JC, CO2 phase fluctuation-induced topological damage enhances shale strength, International Journal of Rock Mechanics and Mining Sciences, Volume 194,2025, https://doi.org/10.1016/j.ijrmms.2025.106206

45. Fondriest, S.A. Smith, G. Di Toro, D. Zampieri, S. Mittempergher. Fault zone structure and seismic slip localization in dolostones, an example from the Southern Alps, Italy

46. Rowe, Å. Fagereng, J.A. Miller, B. Mapani. Signature of coseismic decarbonation in dolomitic fault rocks of the Naukluft Thrust, Namibia. Earth Planet. Sci. Lett., 333 (2012), pp. 200-210

47. Pozzi, M.M. Scuderi, E. Tinti, M. Nazzari, C. Collettini. The role of fault rock fabric in the dynamics of

laboratory faults. J. Geophys. Res.: Solid Earth, 127 (6) (2022), Article e2021JB023779

48. Xie Heping, Jinan Wang, M.A. Kwaśniewski, Multifractal characterization of rock fracture surfaces, International Journal of Rock Mechanics and Mining Sciences, Volume 36, Issue 1, 1999, Pages 19-27, ISSN 1365-1609, https://doi.org/10.1016/S0148-9062(98)00172-7.
49. Eiichi Ishii, Hiroyuki Sanada, Teruki Iwatsuki, Yutaka Sugita, Hiroshi Kurikami, Mechanical strength of the transition zone at the boundary between opal-A and opal-CT zones in siliceous rocks, Engineering Geology, Volume 122, Issues 3–4, 2011, Pages 215-221, ISSN 0013-7952, https://doi.org/10.1016/j.enggeo.2011.05.007.
50. Yamashita, F., Fukuyama, E., Mizoguchi, K., Takizawa, S., Xu, S., & Kawakata, H. (2015). Scale dependence of rock friction at high work rate. Nature, 528(7581), 254-257. doi:10.1038/nature16138
51. Ling, F., Duan, K., Sone, H., & Shang, J. (2025). Mineralogy controls on injection-induced fault slip. Geophysical Research Letters, 52, e2025GL117780. https://doi.org/10.1029/2025GL117780
52. Wells, D. L., & Coppersmith, K. J. (1994). New empirical relationships among magnitude, rupture length, rupture width, rupture area, and surface displacement. Bulletin of the Seismological Society of America, 84(4), 974–1002. https://doi.org/10.1785/bssa0840040974
53. Kanamori, H., & Brodsky, E. E. (2001). The physics of earthquakes. Physics Today, 54(6), 34–40. https://doi.org/10.1063/1.1387590
54. Hanks, T. C., & Bakun, W. H. (2002). A bilinear source-scaling model for M-log A observations of continental earthquakes. Bulletin of the Seismological Society of America, 92(5), 1841–1846. https://doi.org/10.1785/0120010148
55. Somerville, P., Graves, R., Collins, N., Song, S. G., Ni, S., & Cummins, P. (2009). Source and ground motion models for Australian earthquakes. In Proceedings of the 2009 Australian earthquake engineering society conference (pp. 11–13).
56. Ji YL, Wei Wu, Zhihong Zhao, Unloading-induced rock fracture activation and maximum seismic moment prediction, Engineering Geology, Volume 262, 2019, 105352, ISSN 0013-7952, https://doi.org/10.1016/j.enggeo.2019.105352.
57. Wang, L., Kwiatek, G., Renard, F., Guérin-Marthe, S., Rybacki, E., Bohnhof, M., Naumann, M., & Dresen, G. (2024). Fault roughness controls injection-induced seismicity. PNAS, 121(3), e2310039121. https://doi.org/10.1073/pnas.2310039121
58. Casas, G. Mollon, A. Daouadji. DEM analyses of cemented granular fault gouges at the onset of seismic sliding: peak strength, development of shear zones and kinematics. Pure Appl. Geophys., 179 (2) (2022), pp. 679-707
59. Beeler, T.E. Tullis, J.D. Weeks. The roles of time and displacement in the evolution effect in rock friction. Geophys. Res. Lett., 21 (18) (1994), pp. 1987-1990
60. Scuderi, B.M. Carpenter, C. Marone. Physicochemical processes of frictional healing: effects of water on stick-slip stress drop and friction of granular fault gouge. J. Geophys. Res.: Solid Earth, 119 (5) (2014),

pp. 4090-4105

61. Li, M., Niemeijer, A. R., & van Dinther, Y. (2025). Frictional healing and induced earthquakes on conventionally stable faults. Nature Communications, 16(1), 9140.

62. Sirorattanakul, K., Larochelle, S., Rubino, V. et al. Sliding and healing of frictional interfaces that appear stationary. Nature 639, 947–953 (2025). https://doi.org/10.1038/s41586-025-08673-0

63. Okamoto, A., & Vinis, E. (2025). Oscillations in fluid pressure caused by silica precipitation in a fracture. Nature Communications, 16(1), 1791. https://doi.org/10.1038/s41467-025-57199-6

Acknowledgments

The research was funded by the National Natural Science Foundation of China (Grant No. 42672210), the National Science and Technology Major Project of China (Grant No. 2025ZD1403901), and the Hebei Natural Science Foundation (Grant No. D2026203002). All the editors and anonymous reviewers are gratefully acknowledged.

Author contributions

Changliang Wu: Writing – original draft, Methodology, Investigation, Formal analysis, Data curation, Conceptualization.

Yiwen Ju: Writing – original draft, Methodology, Investigation, Formal analysis, Data curation.

Ali Raza: Writing – review & editing, Supervision, Project administration.

Yanjun Lu: Writing – review & editing.

Yu Qi: Writing – review & editing, Supervision, Project administration, Funding acquisition.

Jianchao Cai: Writing – original draft, Methodology, Investigation, Formal analysis, Data curation, Funding acquisition

Hongjian Zhu: Writing – original draft, Methodology, Investigation, Formal analysis, Data curation, Conceptualization.

Declaration of competing interest

The authors declare that they have no known competing financial interests or personal relationships that could have appeared to influence the work reported in this paper.

Supplementary materials

Supplementary material associated with this article can be found in the online version of this article.

Table 1. Specific experimental design.

Sandstone					
LSP			LWP		
Sample ID	Fault dip (°)	Test conditions	Sample ID	Fault dip (°)	Test conditions
LSP-0°	0	δσ1/δt =0.2mm/min	LWP-0°	0	δσ3/δt =0.05MPa/s
LSP-30°	30		LWP-30°	30	
LSP-60°	60		LWP-60°	60	
LSP-90°	90		LWP-90°	90	
Shale					
LSP			LWP		
Sample ID	Fault dip (°)	Test conditions	Sample ID	Fault dip (°)	Test conditions
LSP-0°	0	δσ1/δt =0.2mm/min	LWP-0°	0	δσ3/δt =0.05MPa/s
LSP-30°	30		LWP-30°	30	
LSP-60°	60		LWP-60°	60	
LSP-90°	90		LWP-90°	90	
LWP Sandstone					
Unloading Rate (MPa/s)		Fault dip (°)	Test conditions		
0.01		30	δσ3/δt =0.05MPa/s		
0.02					
0.03					
0.04					
0.05					
0.06					
0.15					

Abbreviations: LSP: load-strengthening path. LWP: load-weakening path. $\delta\sigma_1/\delta t$: loading rate. $\delta\sigma_3/\delta t$: unloading rate.

Table 2. Summary of calculation results.

Sandstone							
LSP				LWP			
Sample ID	Dσd / dt (MPa/s)	M_0	M_W	Sample ID	Dσd / dt (MPa/s)	M_0	M_W
LSP-0°	/	/	/	LWP-0°	/	/	/
LSP-30°	0.029	0.0156	-7.265	LWP-30°	122.725	25.29	-5.125
LSP-60°	0.192	0.0856	-6.772	LWP-60°	88.309	46.56	-4.657
LSP-90°	/	/	/	LWP-90°	/	/	/
Shale							
LSP				LWP			
Sample ID	Dσd / dt (MPa/s)	M_0	M_W	Sample ID	Dσd / dt (MPa/s)	M_0	M_W
LSP-0°	/	/	/	LWP-0°	/	/	/
LSP-30°	1.21	4.8396	-5.603	LWP-30°	26.4	204.5	-4.52
LSP-60°	0.08	0.3359	-6.627	LWP-60°	492.5	90.57	-4.755
LSP-90°	/	/	/	LWP-90°	/	/	/
LWP Sandstone							
Unloading Rate (MPa/s)		Dσd / dt (MPa/s)		M_0		M_W	
0.01		21.2		47.73		-4.94	
0.02		63.27		53.63		-4.906	
0.03		77.25		43.49		-4.967	
0.04		73		53.05		-4.91	
0.05		70		46.57		-4.947	
0.06		75.5		43.18		-4.969	
0.15		60.46		48.03		-4.938	

Abbreviations: Dσd / dt (MPa/s): Stress reduction rate. M_0: Deformation moment. M_W: Moment magnitude.

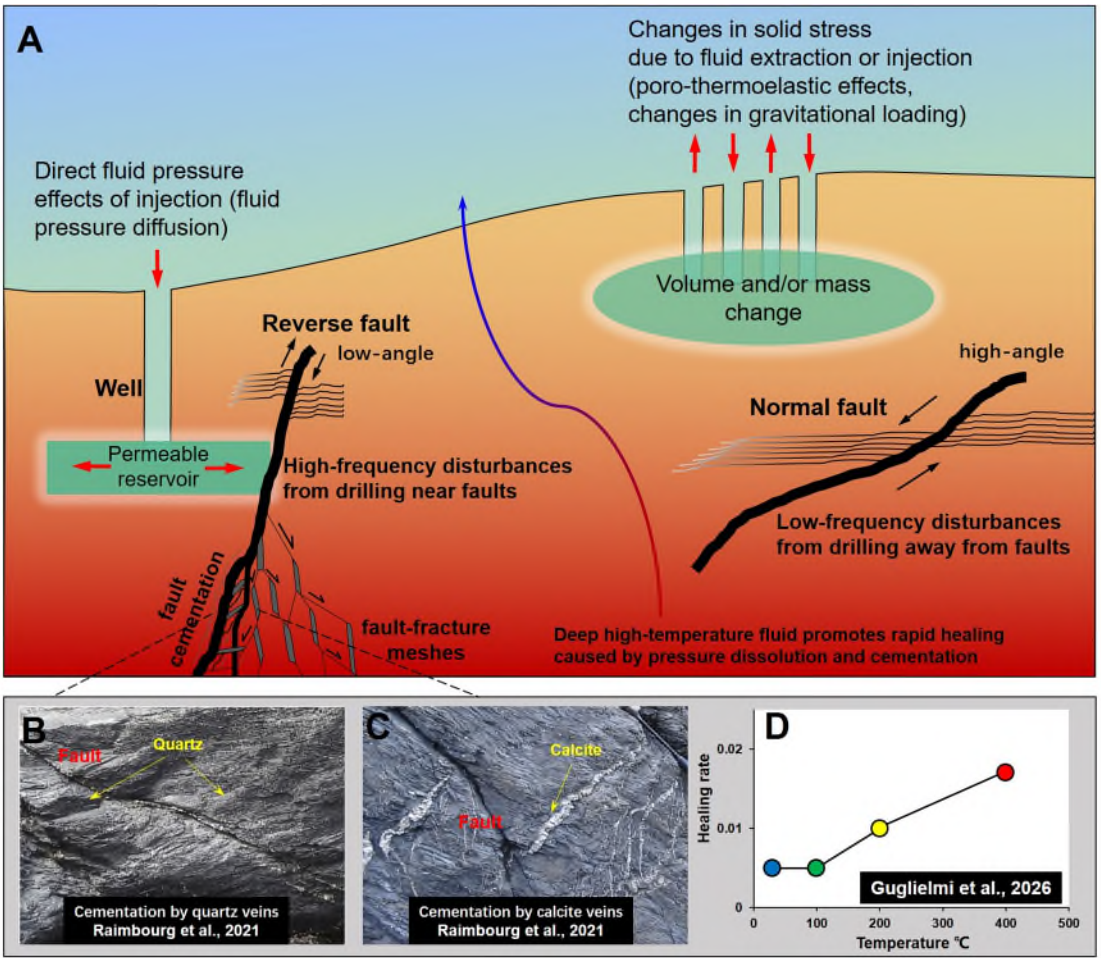


Fig. 1. A：Conceptual models and microstructural evidence of fault healing and reactivation. (A) Schematic diagram of fault healing and reactivation driven by deep hydrothermal upwelling and anthropogenic fluid injection. (B) Quartz-filled veins along a natural fault surface, forming a continuous cement film or bridge that fully occupies the fault plane. (C) Cross-cutting veins in secondary faults: quartz or calcite veins oriented at various angles to the main shear zone; although not fully filling the fault plane, they cross-cut the fault surface and partially cement the adjacent wall rocks. (D) Schematic illustration of accelerated fault healing under elevated temperature.

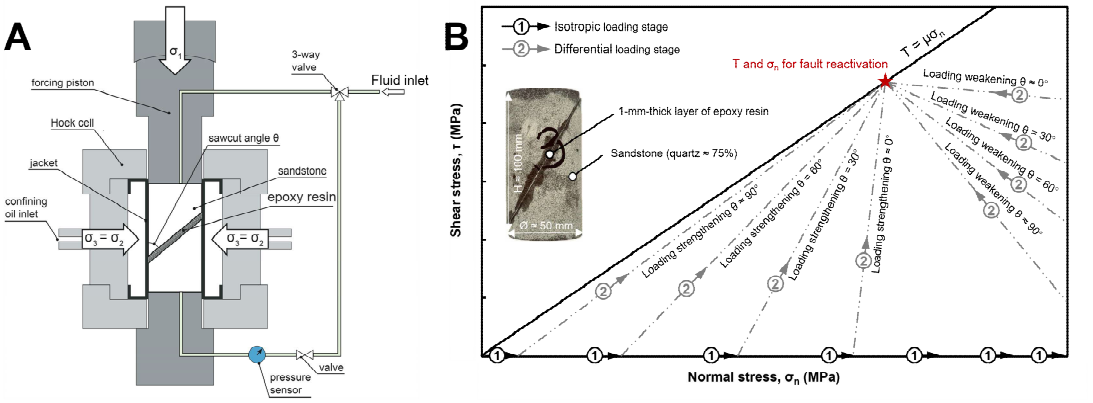


Fig. 2. Experimental setup and loading paths. A. Schematic of the triaxial test system. A loading piston applies vertical (axial) force to the cylindrical specimen, while a Hoek cell delivers isotropic confining pressure via hydraulic oil (Giorgetti, et al., 2021). B. Stress paths applied to the samples. Stage 1: Isotropic loading, increasing the confining pressure to the target value. Stage 2: Differential loading until reactivation occurs—achieved either by increasing the axial pressure (LSP: Loading-Strengthening Path) or by decreasing the confining pressure (LWP: Loading-Weakening Path).

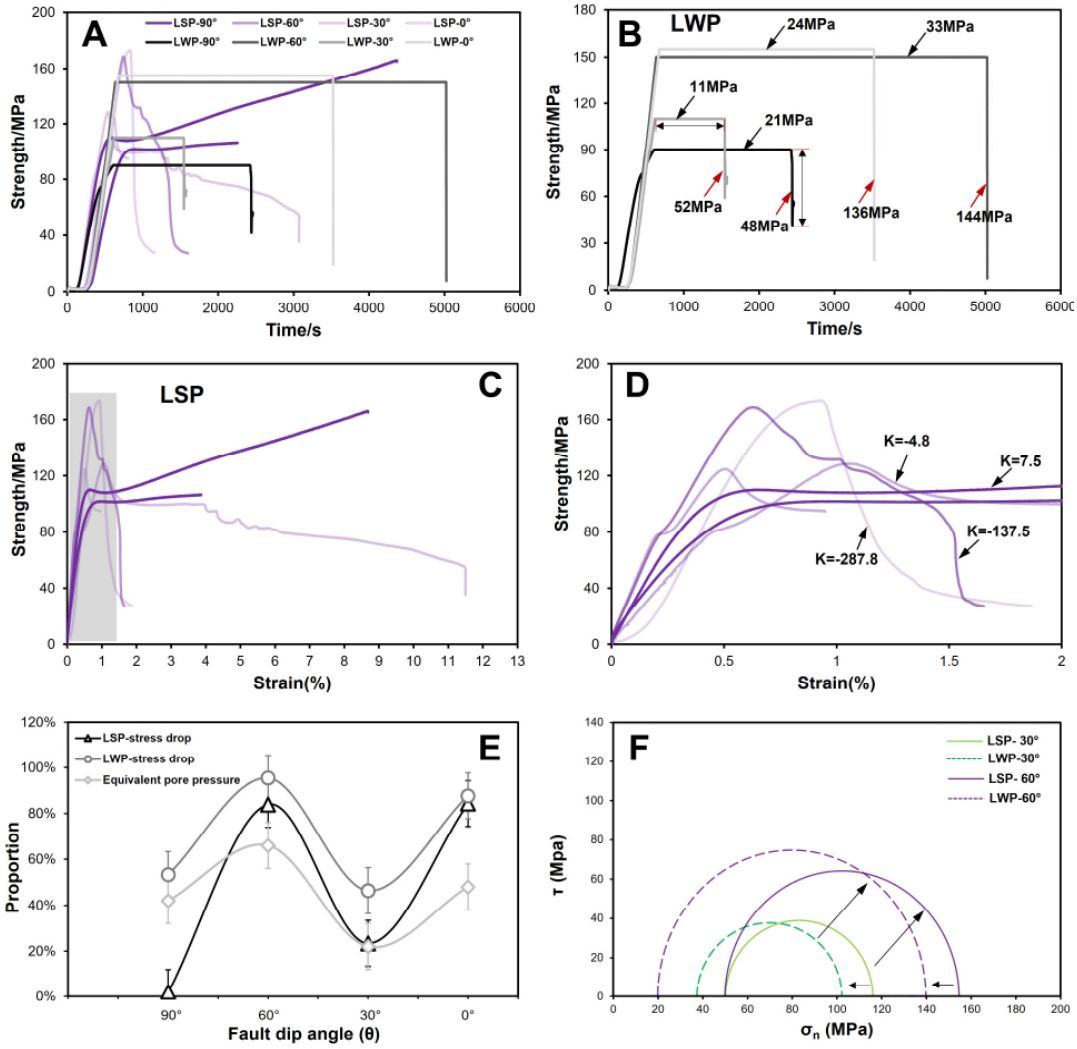


Fig. 3. A–D: Evolution of stress and strain with time for faults subjected to varied stress-path histories. E: Stress-drop magnitude and critical pore pressure as a function of fault dip for different stress paths. F: Mohr-circle evolution under different stress paths.

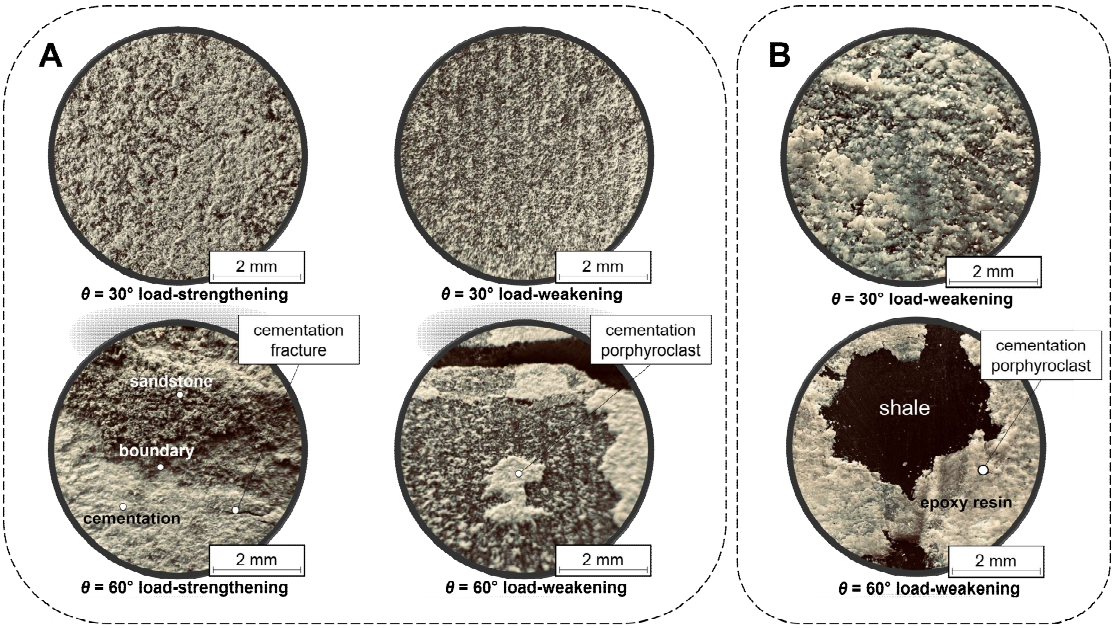


Fig. 4. Microscale failure images of the cemented fault-core material in prefabricated sandstone and shale samples with different dip angles under distinct stress-path histories. A: Micro-scale failure patterns of the cemented sandstone fault core under different stress paths. The 60°-dip fault core exhibits cracking and cataclasis, whereas the 30°-dip core remains relatively intact. B: Micro-scale failure patterns of the cemented shale fault core under different stress paths.

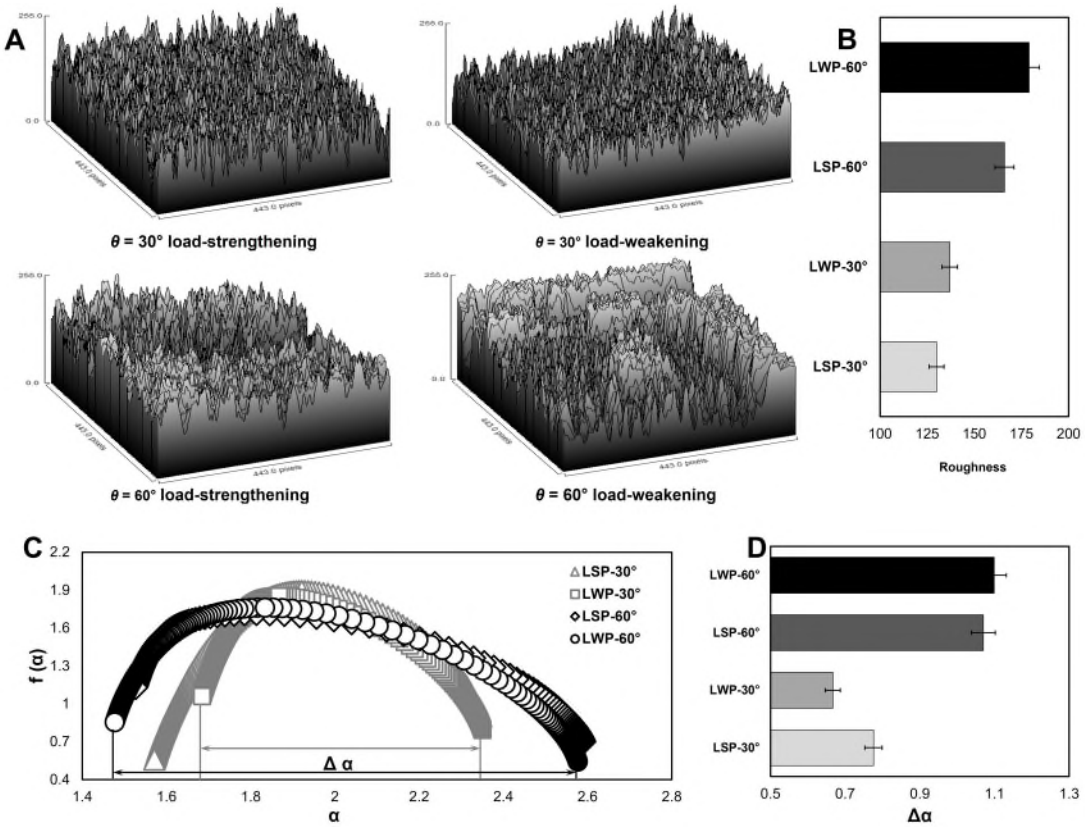


Fig. 5. Quantitative analysis of micro-topographic complexity on prefabricated sandstone fault surfaces with different dip angles under distinct stress-path histories. A: 3D surface-topography extraction. The 30°-dip fault exhibits a more uniform fracture surface, whereas the 60°-dip fault shows pronounced local fragmentation. B: Roughness statistics. The 60°-dip fault surface displays significantly higher roughness than the 30°-dip surface. C: Multifractal spectra of the fracture surfaces. D: Statistics of multifractal-spectrum width. The 30°-dip fault surface has a markedly narrower multifractal spectrum than the 60°-dip surface, indicating more uniform damage within the cement.

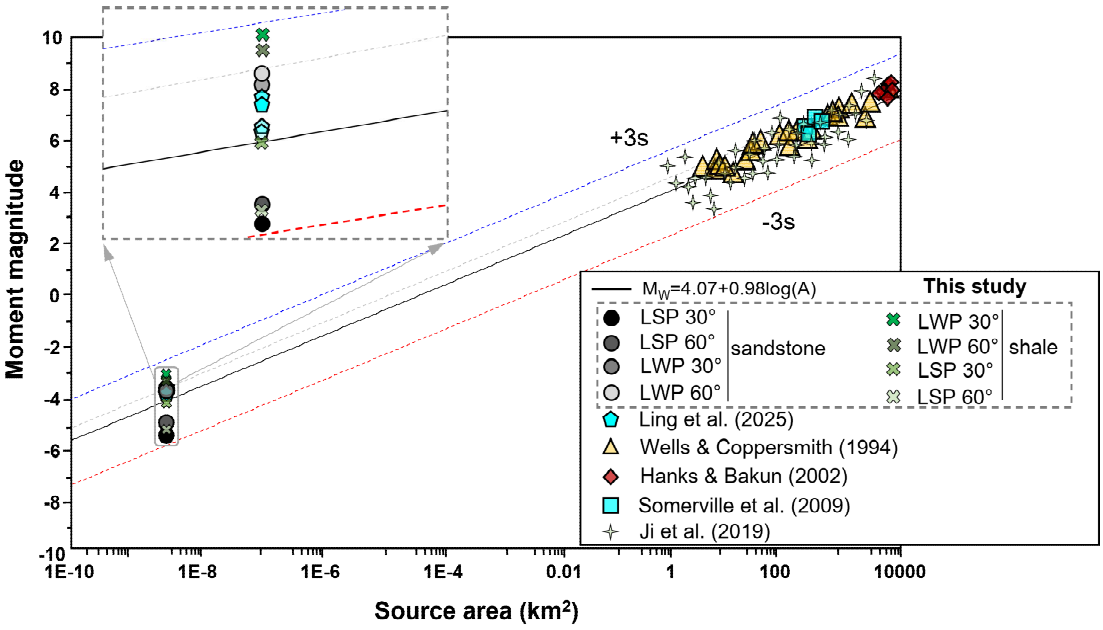


Fig. 6. Moment magnitude as a function of source area. The figure includes laboratory results from this study (sandstone and shale), as well as data compiled from natural and laboratory earthquakes by Wells and Coppersmith (1994), Hanks and Bakun (2002), Somerville et al. (2009), and Ji et al. (2019).

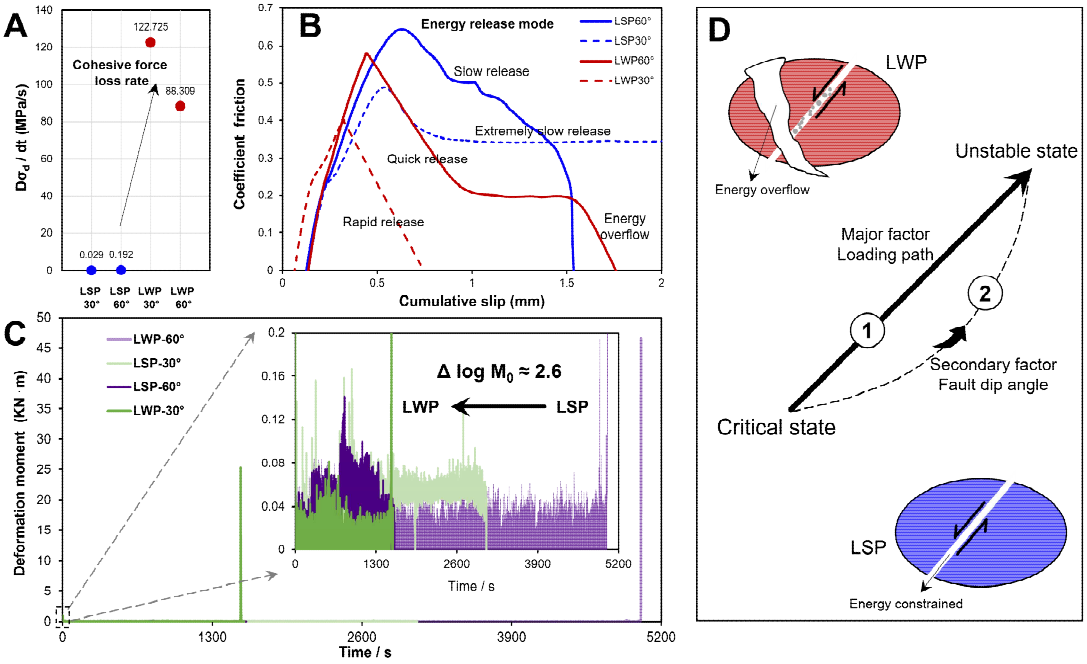


Fig. 7. Seismic potential and mechanism of reactivation for strongly cemented, healed faults under varying dip angles and stress-path histories. A. Rate of cohesion loss within the fault core. B. Evolution of the friction coefficient as a function of slip displacement. C. Temporal evolution of deformation moment. D. Proposed mechanism for the reactivation seismic potential of strongly cemented, healed faults. The stress path dominates the instability scale and can override geometric control. Rapid cohesion loss (LWP) prevents the fault core from dissipating the stored strain energy, forcing energy to spill over into the surrounding rock and generating an exceptionally large seismic moment. In contrast, slow cohesion loss (LSP) confines energy dissipation within the fault core, resulting in a limited seismic moment.

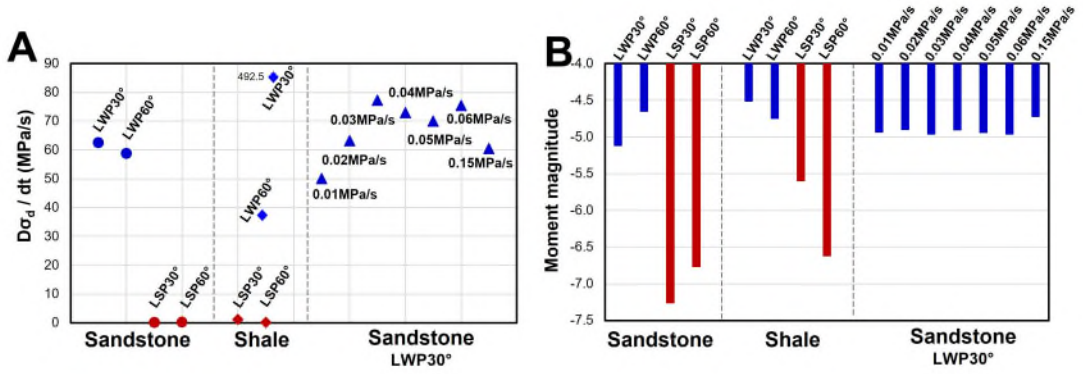


Fig. 8. A: Distribution of stress drop rates for strongly cemented and healed faults under all experimental conditions, including variations in lithology, fault dip angle, stress path, and unloading rate. B: Corresponding distribution of laboratory seismic moments. Regardless of lithology or fault dip angle, the stress drop rate during reactivation of strongly cemented faults under the LWP is significantly higher than that under the LSP, and the seismic moments exhibit the same evolutionary trend. Furthermore, within the range of unloading rates investigated (0.01–0.15 MPa/s), neither the stress drop rate nor the seismic moment is significantly affected by the unloading rate. These results further demonstrate that the stress path governs the seismic potential of strongly cemented fault reactivation by controlling the rate of cohesion loss within the cement.

Supplementary Files

This is a list of supplementary files associated with this preprint. Click to download.

- SupplementaryMaterials925.docx